Commun. Comput. Phys.
doi: 10.4208/cicp.2009.09.016

Vol. 7, No. 2, pp. 362-382
February 2010

Cahn-Hilliard vs Singular Cahn-Hilliard Equations in Phase Field Modeling

Tianyu Zhang[1] and Qi Wang[2,*]

[1] *Department of Mathematical Sciences, Montana State University, Bozeman, MT 59717-2400, USA.*
[2] *Department of Mathematics, University of South Carolina, Columbia, SC 29208, USA.*

Received 5 January 2009; Accepted (in revised version) 26 March 2009

Communicated by Jie Shen

Available online 24 August 2009

Abstract. The Cahn-Hilliard equation is often used to describe evolution of phase boundaries in phase field models for multiphase fluids. In this paper, we compare the use of the Cahn-Hilliard equation (of a constant mobility) for the phase variable with that of the singular or modified Cahn-Hilliard equation (of a variable mobility) in the context of physical derivation of the transport equation and numerical simulations of immiscible binary fluids. We show numerically that (i). both equations work fine for interfaces of small to moderate curvature in short to intermediate time scales; (ii) the Cahn-Hilliard equation renders strong dissipation in simulations of small droplets leading to dissolution of small droplets into the surrounding fluid and/or absorption of small droplets by larger droplets nearby, an artifact for immiscible binary fluids; whereas, the singular Cahn-Hilliard equation can significantly reduce the numerical dissipation around small droplets to yield physically acceptable results in intermediate time scales; (iii) the size of droplets that can be simulated by the Cahn-Hilliard equations scale inversely with the strength of the mixing free energy. Since the intermediate timescale is the time scale of interest in most transient fluid simulations, the singular Cahn-Hilliard equation proves to be the more accurate phase transporting equation for immiscible binary fluids.

AMS subject classifications: 65M06, 76D05, 76A05, 76T30, 76Z05, 92C05

Key words: Cahn-Hilliard equation, phase field, finite difference method, immiscible multiphase flow, singular Cahn-Hilliard equation.

*Corresponding author. *Email addresses:* zhang@math.montana.edu (T. Zhang), qwang@math.sc.edu (Q. Wang)

 ©2010 Global-Science Press

1 Introduction

Modeling and simulating immiscible multiphase fluid flows has been challenging both mathematically and technically. Over the years, various mathematical theories and computational technologies have been developed to tackle the problem. The front tracking method [8], boundary integral method [12], level-set method [16, 19], volume-of-fluid method [11], immersed-boundary method [14,18], and phase field method [1,20–22] have all been proposed, implemented and refined, each of which has shown effectiveness in designated applications. Some of the methods are interconnected while others can be combined to yield more effective computational technologies [13]. Among all above, the phase field method for multiphase fluid flows is perhaps the simplest to implement, given that the phase boundary is embedded in a level set of the phase variable governed by a dissipative evolutionary equation, and physically the most relevant. Because of the ease of use and simplicity, refined details in the formulation of the phase field equation must be well thought out and the free energy, especially, the interfacial free energy for the multiphase fluid must be devised properly to ensure accuracy in numerical computations and fidelity in physical modeling.

In an immiscible binary fluid, the phase field method employs a phase variable $0\leq\phi\leq 1$ to track each phase in the binary fluid: $\phi=1$ describes the region occupied by fluid 1 and $\phi=0$ denotes the one occupied by fluid 2 while $0<\phi<1$ describes the interfacial region. The phase variable is also known as the labeling function by some. The time evolution of the phase variable ϕ is governed according to the Cahn-Hilliard equation [4, 5]

$$\frac{d\phi}{dt}=\nabla\cdot(\lambda\nabla\mu), \tag{1.1}$$

where λ is the mobility and μ is the chemical potential of the multiphase fluid system, a functional of the phase variable ϕ. The phase variable ϕ can be identified with the volume fraction of fluid 1; so, $1-\phi$ serves as the volume fraction of fluid 2. In this formulation of the transport equation for ϕ, the flux of ϕ is assumed to be proportional to the force due to the prescribed chemical potential. However, a more physically appropriate assumption is to assume the transporting velocity of ϕ is proportional to the force due to the chemical potential, a consequence of the friction dynamics [3, 6]. This leads to the singular or modified Cahn-Hilliard equation

$$\frac{d\phi}{dt}=\nabla\cdot(\lambda_s\phi\nabla\mu), \tag{1.2}$$

where λ_s is the mobility. The effective mobility is $\lambda=\lambda_s\phi$ in the singular Cahn-Hilliard equation. It vanishes in fluid 2. If we assume mixing only goes on in the interfacial layer, it would be reasonable to assume $\lambda_s=\lambda_s^1(1-\phi)$, where λ_s^1 is a constant. Hence, the effective mobility is $\lambda=\lambda_s^1\phi(1-\phi)$. In the classical Cahn-Hilliard equation, the mobility is a constant, whereas it is a phase variable dependent function in the modified case.

The phase field model, also known as the diffuse interface method, benefits from the dissipation mechanism in the equation. There exists a interfacial layer in which two fluids mix due to dissipation. Outside the layer, it is expected to maintain a constant value for the phase variable ϕ in the fluid. For spatially slow varying interfaces, namely, the one of small to intermediate curvature, phase field models yield acceptable interfaces with thickness controlled within a few grid size. When the curvature is large, resolving the interface and interfacial layer correctly becomes challenging.

In this paper, we will compare numerical simulations of two droplets of fluid 1 immersed in fluid 2 using the Cahn-Hilliard equation and the singular Cahn-Hilliard equations, respectively, to discuss their efficacy in phase field modeling for immiscible binary fluids. We name the singular Cahn-Hilliard equation of $\lambda=\lambda_s^1\phi(1-\phi)$ MCH 1 to differentiate it from the modified Cahn-Hilliard (MCH) equation (1.2). We will show through numerical simulations that the singular Cahn-Hilliard equation yields better numerical resolution and less interface dislocation compared to the classical Cahn-Hilliard equation in simulations of immiscible droplets. This is because the singular Cahn-Hilliard equation is more physically relevant to the interfacial problem and tends to annihilate dissipation and mixing outside the interfacial layer. In the remaining sections of the paper, we first present the full flow-interface coupled equation system and its dimensionless form; then, we briefly discuss the numerical method used in the simulations; finally, we present our simulation results and discussions.

2 Mathematical models

We consider a binary fluid of two immiscible viscous fluids. The binary fluid is assumed incompressible. We use a phase variable ϕ to label each fluid:

$$\phi=\begin{cases} 1, & \text{in fluid 1,} \\ 0, & \text{in fluid 2.} \end{cases} \tag{2.1}$$

We denote the average velocity by $\mathbf{v}$. The transport equation for the mass and momentum is given respectively by

$$\nabla\cdot\mathbf{v}=0, \tag{2.2a}$$

$$\rho\frac{d\mathbf{v}}{dt}=\nabla\cdot(\phi\tau_1+(1-\phi)\tau_2)-[\nabla p+\gamma_1 k_B T\nabla\cdot(\nabla\phi\nabla\phi)], \tag{2.2b}$$

where $\rho=\phi\rho_1+(1-\phi)\rho_2$ is the effective density for the binary fluid, p is the pressure, ρ_1, τ_1 and ρ_2, τ_2 are the density and the extra stress tensor for viscous fluid 1 and 2, respectively, k_B is the Boltzmann constant, T is the temperature, γ_1 is a parameter measuring the strength of the conformation entropy and γ_2 is the strength of the bulk mixing free energy in the "mixing free energy density" [7,9] defined by

$$f=\frac{\gamma_1}{2}k_B T\|\nabla\phi\|^2+\gamma_2 k_B T\phi^2(1-\phi)^2. \tag{2.3}$$

In the Cahn-Hilliard equations, the velocity of fluid 1 is defined by

$$\mathbf{v}_1 = \mathbf{v} - \frac{\lambda}{\phi}\nabla\frac{\delta f}{\delta\phi}. \tag{2.4}$$

and that of fluid 2 is given by

$$\mathbf{v}_2 = \mathbf{v} + \frac{\lambda}{1-\phi}\nabla\frac{\delta f}{\delta\phi}, \tag{2.5}$$

where λ takes on a specific form in CH, MCH, MCH1 model, respectively. The extra stress tensors are given by

$$\tau_1 = 2\eta_1\mathbf{D}, \qquad \tau_2 = 2\eta_2\mathbf{D}, \tag{2.6}$$

where η_1,η_2 are the viscosity for fluid 1 and 2, respectively, $\mathbf{D}$ is the rate of strain tensor for the mixture associated to the average velocity $\mathbf{v}$ defined by

$$\mathbf{D} = \frac{1}{2}[\nabla\mathbf{v} + \nabla\mathbf{v}^T].$$

We investigate the interfacial dynamics of the immiscible binary fluid in 2 space dimensions here: $(x,y)\in\Omega=[0,L]\times[0,H]$, where H and L are positive constants. At the boundary of the fixed domain $\partial\Omega$, we impose no-flux boundary conditions for the phase variable of fluid 1, which can be effectively viewed as the volume fraction of fluid 1, Dirichlet boundary condition for the velocity:

$$\nabla\phi\cdot\mathbf{n}|_{\partial\Omega} = 0, \tag{2.7a}$$

$$[\mathbf{v}\phi - \lambda\nabla\frac{\delta f}{\delta\phi}]\cdot\mathbf{n}|_{\partial\Omega} = 0, \tag{2.7b}$$

$$\mathbf{v}|_{\partial\Omega} = 0. \tag{2.7c}$$

We use a characteristic time scale t_0 and length scale $h=H$ to nondimensionalize the variables

$$\tilde{t} = \frac{t}{t_0}, \quad \tilde{\mathbf{x}} = \frac{\mathbf{x}}{h}, \quad \tilde{\mathbf{v}} = \frac{\mathbf{v}t_0}{h}, \quad \tilde{p} = \frac{pt_0^2}{\rho_0 h^2}, \quad \tilde{\tau}_i = \frac{\tau_i t_0^2}{\rho_0 h^2}, \quad i=1,2. \tag{2.8}$$

The length scale h is determined by the computational geometry while the time scale is done by either the growth time scale of the interface or a flow induced time scale. The following dimensionless equations arise

$$\begin{aligned} &\Lambda = \frac{\lambda\rho_0}{t_0}, \quad \Gamma_1 = \frac{\gamma_1 k_B T t_0^2}{\rho_0 h^4}, \quad \Gamma_2 = \frac{\gamma_2 k_B T t_0^2}{\rho_0 h^2}, \\ &Re_2 = \frac{\rho_0 h^2}{\eta_2 t_0}, \quad Re_1 = \frac{\rho_0 h^2}{\eta_1 t_0}, \quad \tilde{\rho} = \phi\frac{\rho_1}{\rho_0} + (1-\phi)\frac{\rho_2}{\rho_0}, \end{aligned} \tag{2.9}$$

where Re_1 and Re_2 are the Reynolds number for fluid 1 and fluid 2, respectively, ρ_0 is an average (or a constant reference) density. For simplicity, we drop the ˜ on the dimensionless variables and the parameters. The system of governing equations for the binary fluid in these dimensionless variables are given by

$$\nabla\cdot(\mathbf{v})=0, \tag{2.10a}$$

$$\rho\frac{d\mathbf{v}}{dt}=\nabla\cdot(\phi\tau_1+(1-\phi)\tau_2)-[\nabla p+\Gamma_1\nabla\cdot(\nabla\phi\nabla\phi)], \tag{2.10b}$$

$$\frac{\partial\phi}{\partial t}+\nabla\cdot(\phi\mathbf{v})=\nabla\cdot(\Lambda\nabla\frac{\delta f}{\delta\phi}), \tag{2.10c}$$

where

$$\tau_1=\frac{2}{Re_1}\mathbf{D},\quad \tau_2=\frac{2}{Re_2}\mathbf{D},\quad \Lambda=\text{const}\,(CH),$$
$$\Lambda\to\Lambda\phi\,(MCH),\quad \Lambda\to\Lambda\phi(1-\phi)\,(MCH1).$$

The mixing free energy density is now given by

$$f=\frac{\Gamma_1}{2}\|\nabla\phi\|^2+\Gamma_2\phi^2(1-\phi)^2. \tag{2.11}$$

Notice that constant $\phi=\phi_0$ and $\mathbf{v}=\mathbf{v}_0$ yield a solution of the governing system of equations. If we linearize the system about the constant solution and examine the linear growthrate associated with the phase variable ϕ, we arrive at the growth rate:

$$\sigma=\Lambda(\phi_0)\beta^2\Big(\Gamma_2\frac{\partial^2 f}{\partial\phi^2}-\Gamma_1\beta^2\Big), \tag{2.12}$$

where β is the wave number and $\tilde{f}=\Gamma_2\phi^2(1-\phi)^2$. The growth rate can be positive if $\partial^2\tilde{f}/\partial\phi^2>0$. This is true when

$$0\le\phi<\frac{3-\sqrt{3}}{6}\quad\text{or}\quad\frac{3+\sqrt{3}}{6}<\phi\le 1.$$

The cutoff wave number in the case of positive growth is given by

$$\beta=\sqrt{\frac{\Gamma_2}{\Gamma_1}\frac{\partial^2\tilde{f}}{\partial\phi^2}}. \tag{2.13}$$

At $\phi_0=0,1$,

$$\beta=\sqrt{2\Gamma_2/\Gamma_1}. \tag{2.14}$$

The corresponding growth rate at $\phi_0=0,1$ is

$$\sigma=\Lambda(\phi_0)\Gamma_1\beta^2\Big(\frac{2\Gamma_2}{\Gamma_1}-\beta^2\Big). \tag{2.15}$$

In most applications, $\Gamma_1 \ll \Gamma_2$, the growth or decay rate is dominated by the value of $\Lambda\Gamma_2\beta^2$ for long waves or the value of $-\Lambda\Gamma_1\beta^4$ for shortwaves. For the singular Cahn-Hilliard models, MCH, the linear growth and decay rate at $\phi=0$ is zero; so is the growth rate of MCH1 at $\phi_0=1$. Hence, the linear growth at the bulk phase of fluid 1 and 2 vanishes in the MCH models in contrast to a positive one in the CH model. This simple linear stability analysis may shed light on the potentially significant dissipation around small scale spatial structures in the immiscible binary fluid due to numerically induced disturbances.

3 Numerical schemes

We use a finite difference method to solve the coupled flow and phase field equation [23]. We solve the coupled momentum transport equation and the continuity equation using a Gauge-Uzawa method developed by Pyo and Shen [10]. With

$$\mathbf{R}=-\nabla\cdot(\Gamma_1\nabla\phi\nabla\phi)+\nabla\cdot\Big(\phi\tau_1+(1-\phi)\tau_2-\frac{2}{Re_a}\mathbf{D}\Big), \tag{3.1}$$

where Re_a is an averaged Reynolds number, the momentum transport equation can be rewritten as

$$\rho\Big(\frac{\partial}{\partial t}\mathbf{v}+\mathbf{v}\cdot\nabla\mathbf{v}\Big)=-\nabla p+\frac{1}{Re_a}\nabla^2\mathbf{v}+\mathbf{R}. \tag{3.2}$$

We calculate $\mathbf{v}$ and the pressure in three steps. For simplicity, the second order extrapolation in time of any function f is denoted by

$$\overline{f}^{n+1}=2f^n-f^{n-1}.$$

Step 1:

$$\begin{cases} \rho^{n+1}\Big[\dfrac{3\mathbf{u}^{n+1}-4\mathbf{v}^n+\mathbf{v}^{n-1}}{2\Delta t}\Big]+\rho^{n+1}\overline{\mathbf{v}}^{n+1}\cdot\nabla\mathbf{u}^{n+1}+\nabla p^n+\dfrac{1}{Re_a}[\nabla s^n-\nabla^2\mathbf{u}^{n+1}]=\overline{\mathbf{R}}^{n+1}, \\ \mathbf{u}^{n+1}|_{\partial\Omega}=0. \end{cases} \tag{3.3}$$

Step 2: We implement the projection step by solving a Poisson equation with the Neumann boundary condition:

$$\begin{cases} -\nabla\cdot\Big(\dfrac{1}{\rho^{n+1}}\nabla\psi^{n+1}\Big)=\nabla\cdot\mathbf{u}^{n+1}, \\ \dfrac{\partial\psi^{n+1}}{\partial n}|_{\partial\Omega}=0. \end{cases} \tag{3.4}$$

Step 3: We correct the velocity, pressure and the auxiliary variable s.

$$\begin{cases} \mathbf{v}^{n+1}=\mathbf{u}^{n+1}+\dfrac{1}{\rho^{n+1}}\nabla\psi^{n+1}, \\ s^{n+1}=s^n-\nabla\cdot\mathbf{u}^{n+1}, \\ p^{n+1}=p^n-\dfrac{3\psi^{n+1}}{2\Delta t}+\dfrac{1}{Re_a}s^{n+1}. \end{cases} \tag{3.5}$$

Here $s^0=0$ and $\mathbf{v}^1,s^1,p^1,\phi^1,c^1$ are computed by a first order scheme.

The phase field equation for the polymer volume fraction ϕ is discretized by

$$\begin{aligned} &\frac{3\phi^{n+1}-4\phi^n+\phi^{n-1}}{2\Delta t}+\mathbf{v}^{n+1}\cdot\nabla\phi^{n+1} \\ &=\nabla\cdot\Lambda(\overline{\phi}^{n+1})\left[\nabla\left(-\Gamma_1\nabla^2\phi^{n+1}+2\Gamma_2(\phi^{n+1}-3(\overline{\phi}^{n+1})^2+2(\overline{\phi}^{n+1})^3)\right)\right]. \end{aligned} \tag{3.6}$$

The spatial discretization is done using central differences to ensure at least second order accuracy in space.

We use uniform mesh size in both space and time, where the time step size is Δt and spatial mesh size is $\Delta x=L/M_x,\Delta y=H/M_y$, respectively. The computation domain $\Omega=[0,L]\times[0,H]$ is divided into uniform cells by nodes $(x_i,y_j)=(i\Delta x,j\Delta y),i=0,\cdots,M_x,j=0,\cdots,M_y$. we denote the value of the numerical solution of (3.6) at $(n\Delta t,i\Delta x,j\Delta y)$ by $\phi^n_{i,j}$. Given that $\mathbf{v}\cdot\mathbf{n}|_{\partial\Omega}=0$. The boundary condition for ϕ given by (2.7) becomes

$$\nabla\phi\cdot\mathbf{n}|_{\partial\Omega}=0,\quad \nabla\frac{\delta f}{\delta\phi}\cdot\mathbf{n}|_{\partial\Omega}=0. \tag{3.7}$$

The discrete forms of the boundary conditions (3.7) at $y=0,H$ are given by

$$\phi^n_{i,1}=\phi^n_{i,-1},\ \phi^n_{i,2}=\phi^n_{i,-2},\ \phi^n_{i,M_y+1}=\phi^n_{i,M_y-1},\ \phi^n_{i,M_y+2}=\phi^n_{i,M_y-2},\quad i=0,\cdots,M_x. \tag{3.8}$$

The boundary conditions at $x=0,L$ are discretized analogously.

The overall scheme is second order in space and time. To achieve second order accuracy in time, extrapolation is used for the $\mathbf{R}$ term in momentum transport equation (3.3) and the nonlinear terms in the phase filed equation (3.6). The density of fluid 1 and 2 are set to be the same in this paper; thus ρ^n is in fact a constant. The averaged Reynolds number Re_a is computed by

$$Re_a=\phi^n_{\max}Re_1+(1-\phi^n_{\max})Re_2, \tag{3.9}$$

where $\phi^n_{\max}=\max\{\phi^n_{i,j},0\le i\le M_x,0\le j\le M_y\}$. Thus Re_a is a constant at each time step t_n, but varies with time. Eqs. (3.3) and (3.4) are solved using a fast Poisson solver based on FFT while Eq. (3.6) is solved using the GMRES method. We remark that given the

magnitude of the mobility coefficient used in the simulation, the condition number of the coefficient matrix in the discretized system is manageable. Otherwise, a preconditioner based on the linear part of the system with a constant mobility can be used to improve the convergence.

We run the mesh refinement test for $\Delta x=\Delta y=1/32,1/64,1/128,1/256$ respectively and the results show second order error reduction in both time and space. All numerical results presented here are obtained with $\Delta x=\Delta y=1/128$, except for the study of two small droplets where $\Delta x=\Delta y=1/256$.

4 Numerical results and discussions

We study dynamics of droplets of fluid 1 immersed in fluid 2. We assume fluid 1 is much more viscous than fluid 2. The dimensionless parameters are set at

$$\begin{aligned} &Re_2=9.98\times10^{-4},\quad Re_1=2.33\times10^{6},\quad \Lambda=1\times10^{-9},\\ &\Gamma_1=292.8,\quad \Gamma_2=2.5\times10^{6},\quad L=2,\quad H=1. \end{aligned} \tag{4.1}$$

We simulate dynamics of droplets of fluid 1 in a matrix of fluid 2 using both the Cahn-Hilliard and the modified or singular Cahn-Hilliard equations. We first simulate two droplets of fluid 1 of radius ratio 5:1 immersed in fluid 2 using the Cahn-Hilliard equation in a rectangular domain Ω. Fig. 1 is the contour plot of a few snapshots of ϕ at selected time, in which the two droplets begin with initial radius ratio 5:1. As time evolves, the value of ϕ in the smaller droplet reduces while its center remains unchanged. Beyond $t=50$, the value reduces to a nearly zero value so that the smaller droplet disappears visually. This numerical phenomenon was also observed in the simulation by others using the Cahn-Hilliard model [15]. It is certainly an amplification of the higher order dissipation in the numerical treatment of the equation. For two immiscible fluids, there is no mathematical nor physical evidence to support the numerical phenomenon seen here, in which the larger droplet seemingly overtakes the smaller one in intermediate time scales for volume ratio 5:1. We notice that right after the smaller droplet disappears visibly at $t=50$, the right boundary (the side facing the smaller droplet) of the larger droplet bulges outward; during the time period from $t=50$ to $t=80$, the large droplet recovers its circular shape due to surface tension. The well-known Ostwald ripening observed for solid in solution or one liquid in another liquid is closely related to the above simulation. However, it normally occurs at much larger volume ratios or at longer time scales [17].

By switching to the modified Cahn-Hilliard equations while retaining all the same model parameters, the numerical phenomenon that the larger droplet overtakes the smaller one is significantly delayed in the time scale shown in Fig. 2. Since the flux is modified by ϕ itself in MCH and $\phi(1-\phi)$ in MCH1, we see that the numerical dissipation in this model is much weaker than in the CH model so that each droplet keeps its original position and size after long time (say, $t=80$). The results obtained by MCH or

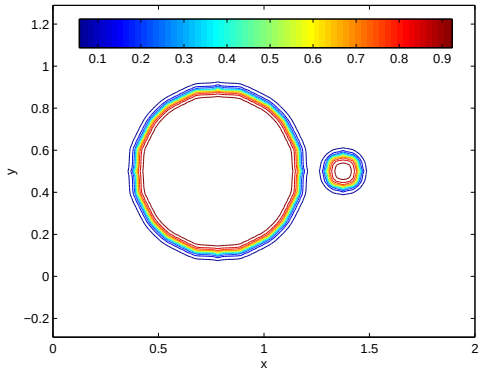

(a) t = 0

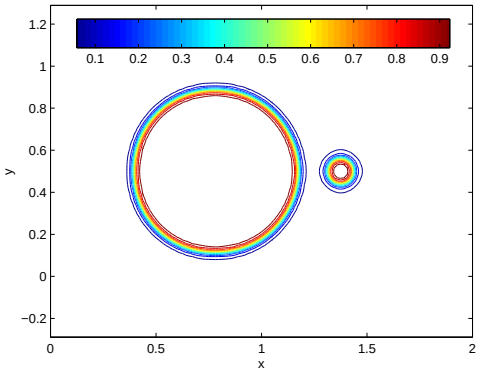

(b) t =20

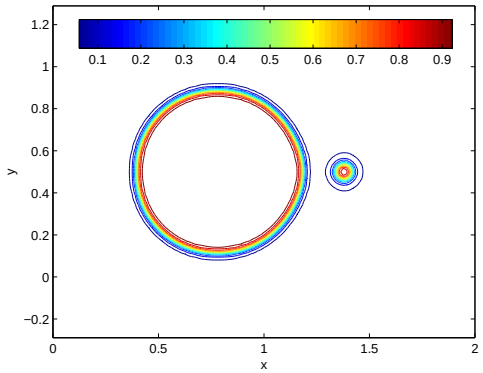

(c) t = 40

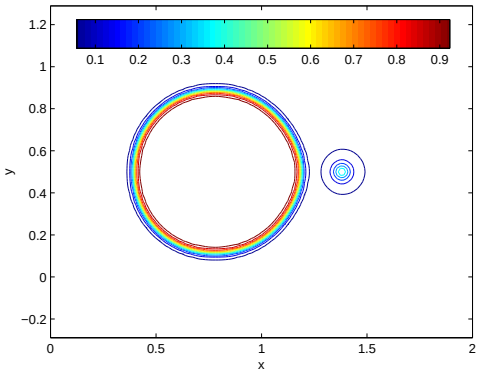

(d) t = 45

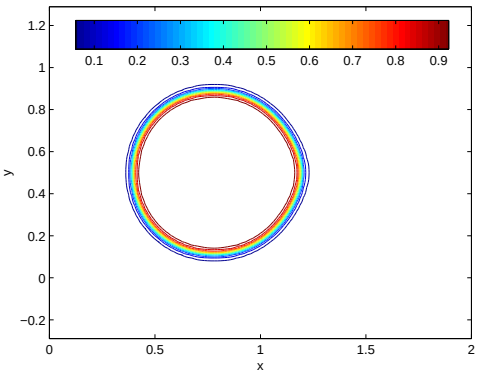

(e) t = 50

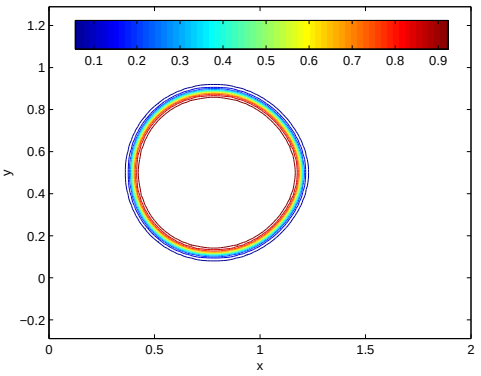

(f) t = 80

Figure 1: Contour plots of two droplets with initial radius ratio 5:1 at selected time slots, where the CH model is used.

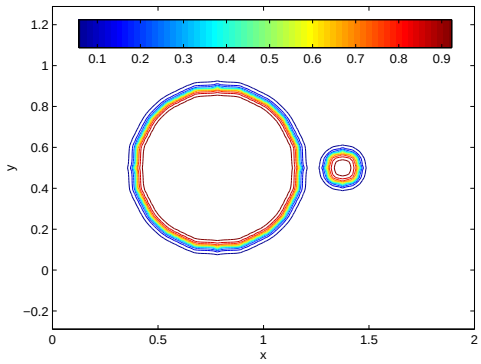

(a) t = 0

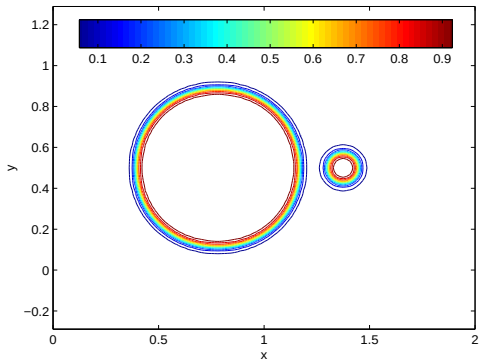

(b) t =80

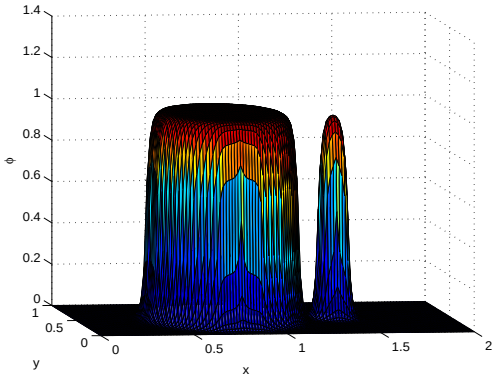

(c) t = 0

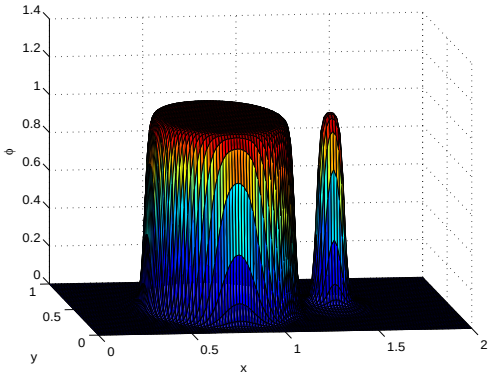

(d) t =80

Figure 2: (a)-(b). Contour plots of two droplets with initial radius ratio 5:1, where the MCH model is used. (c)-(d). Profiles of phase variable ϕ for two droplets depicted in (a) and (b).

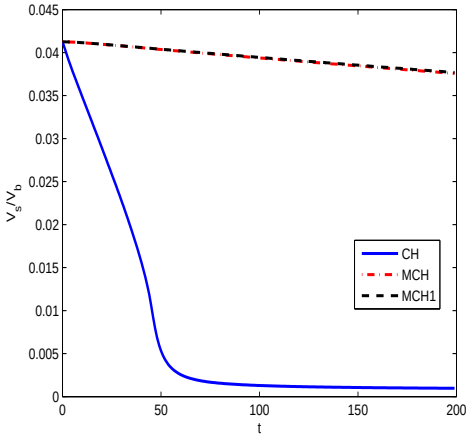

Figure 3: Volume ratio of the smaller to the bigger droplet versus time, where the initial radius ratio is 1:5.

MCH1 are nearly identical. These simulations show that the MCH models clearly render much smaller numerical dissipation and give better resolution in the immiscible droplet simulation than the CH model does.

To document the time scale in which the smaller droplet shrinks (or dissolves) to extinction, we calculate the volume ratio of the smaller droplet to the larger one. Fig. 3 shows the volume ratio of the small to large droplet versus time. For the CH model, it decreases fast linearly up to $t\approx 40$, then it decreases even faster up to $t\approx 50$; after that, the decreasing rate becomes much smaller and reaches equilibrium around $t=100$ where the value of the phase variable becomes numerically insignificant outside the large drop. We note that the volume ratio never drops to zero in the range of our numerical computations since ϕ starts out positive in the original position of the smaller droplet. For both MCH models, the volume ratio decreases linearly in our numerical computations with a much slower rate; it drops less than 10% at $t=80$.

Now that the mass in the smaller droplet is transported into the larger one and the surrounding fluid 2 in finite time in the phase filed models, we calculate the value of ϕ and the flux to investigate how the transport is carried out. Fig. 4 shows the profile of ϕ between two droplets at $t=40$, where both the CH and the MCH model have a positive value of ϕ, forming a saddle shaped profile or bridge between the two droplets. The bridge for the CH model is slightly higher than the one for the MCH models. Besides the profile of ϕ, we also calculate the transport flux shown in Fig. 4, which depicts the components of flux due to the gradient of the chemical potential for the CH model and the MCH model, respectively. Even though they have similar profile, the flux of the CH model is 2 orders of magnitude larger than that of the MCH model ($\mathcal{O}(10^{-3})$ vs $\mathcal{O}(10^{-5})$). We note that the numerical results of MCH and MCH1 are comparable in all cases we computed in this study. We thus focus on the comparison between the CH and the MCH model only in the following.

The reduced transport flux in the case of the MCH models is the key for the much delayed mass dissipation and volume-reduction in the smaller droplet in the numerical experiment. By zooming in on the detail of the flux vector in the case of the CH model, we notice the difference in flux patterns: the flux coming out of the smaller droplet dissipates to all directions initially but converge to the direction of the larger droplet at later times; whereas the weaker dissipation into all directions is observed in the case of the MCH models in the time period we computed. Fig. 5 depicts the vector field plot of the flux for the CH model at selected time slots. On the left are the plots in the whole domain, on the right are the zoom-in plots around the most active region. For t = 40, 50, significant flux activities are around the smaller droplet causing dissipation in all directions. The transport to the left is slightly stronger, leading to the bridge shown previously. At t = 80, absorption is nearly complete, so significant flux activities appear on the right boundary of the bigger droplet, correlating to its recovery of the original circular shape. Fig. 6 shows the vector field plot of the flux for the MCH model at different time. At t = 40, 50, 80, significant flux activities all appear around the smaller droplet and causes dissipation in all directions. But the transport is much weaker, corroborated by Figs. 3 and 4.

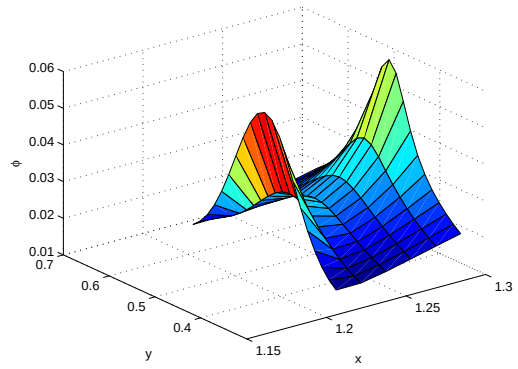

(a) CH

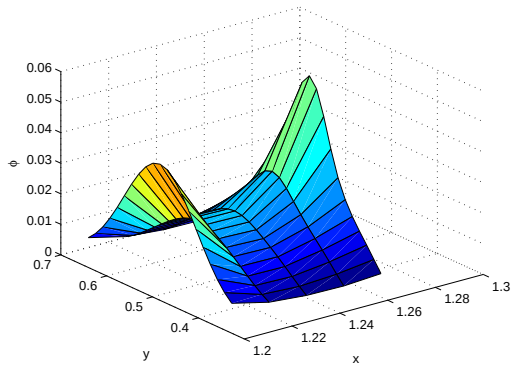

(b) MCH, mobility $\lambda\phi$

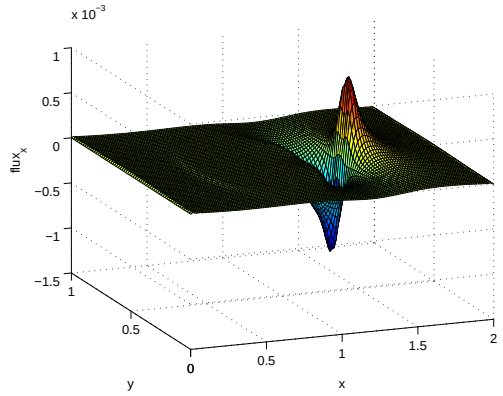

(c) CH, x flux

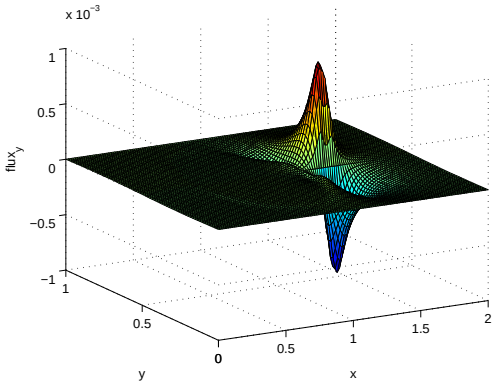

(d) CH, y flux

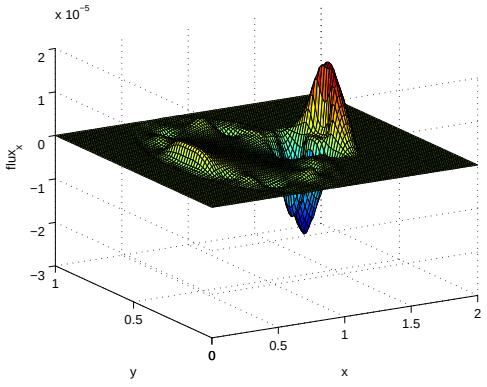

(e) MCH, x flux

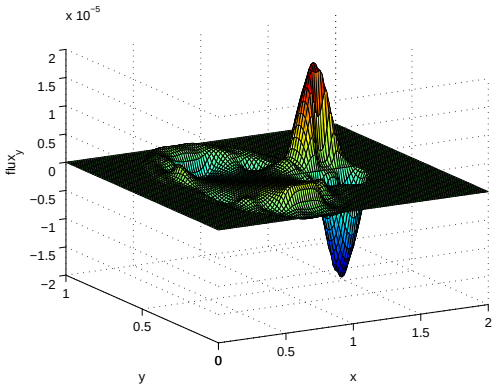

(f) MCH, y flux

Figure 4: Saddle shaped profile or bridge of ϕ between two droplets at $t=40$ with initial radius ratio 5:1 in (a) and (b). Flux components due to chemical potential gradient at $t=40$ with initial radius ratio 5:1 in (c-f). The flux$=-\Lambda\nabla\frac{\delta f}{\delta\phi}$.

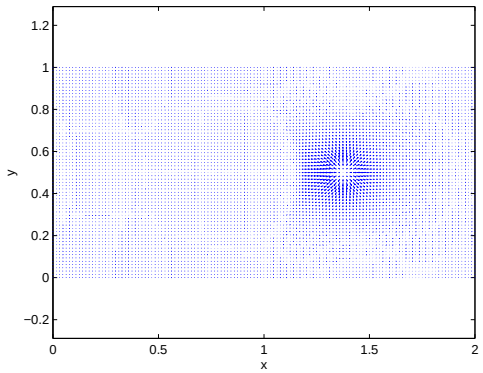

(a) t = 40, whole domain

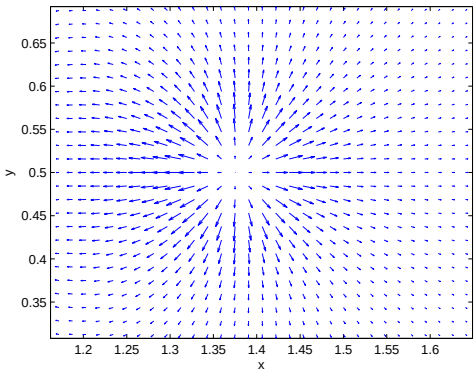

(b) t =40, zoom in

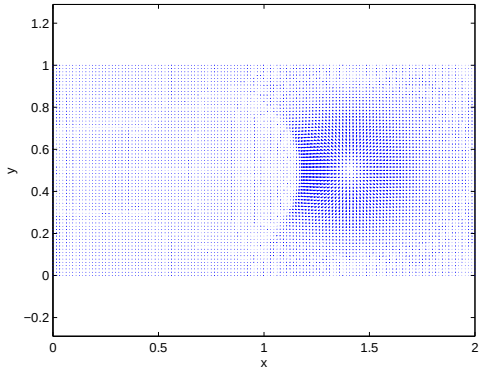

(c) t = 50, whole domain

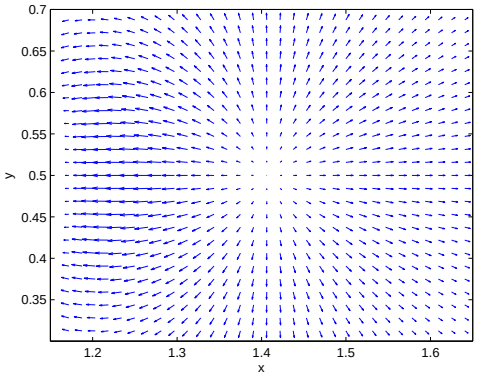

(d) t = 50, zoom in

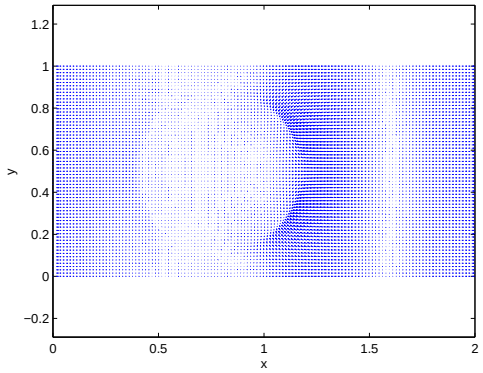

(e) t = 80, whole domain

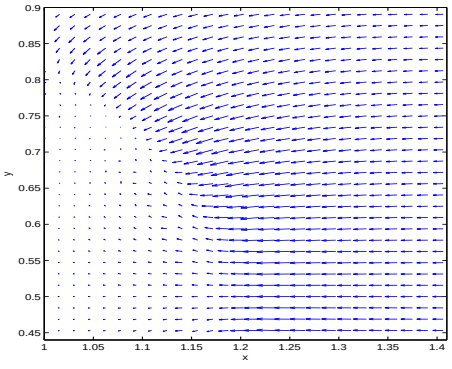

(f) t = 80, zoom in

Figure 5: Flux vector due to chemical potential gradient with initial radius ratio 5:1. The result is obtained from the CH model.

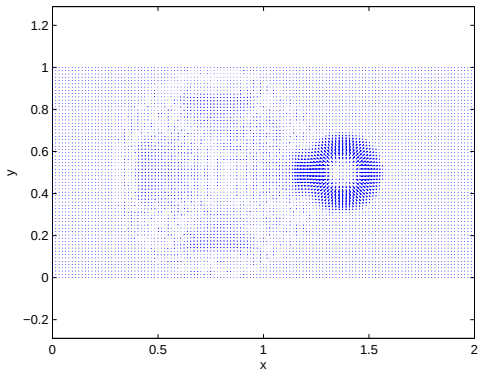

(a) t = 40, whole domain

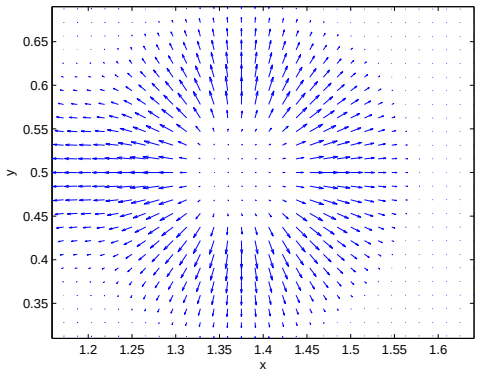

(b) t =40, zoom in

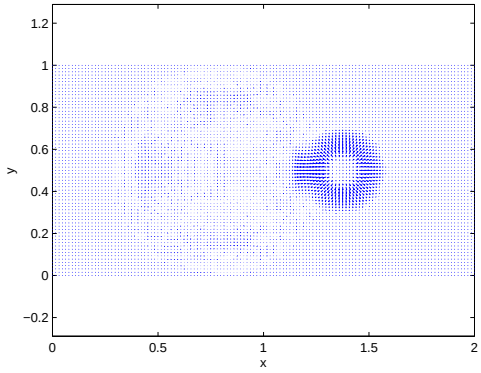

(c) t = 50, whole domain

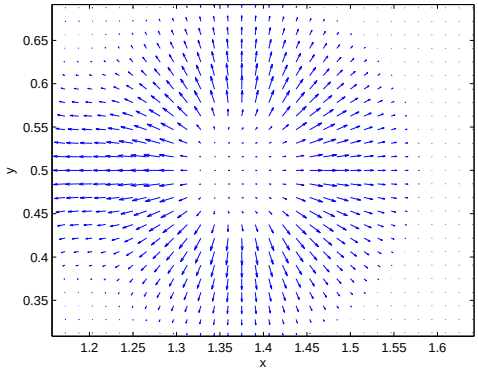

(d) t = 50, zoom in

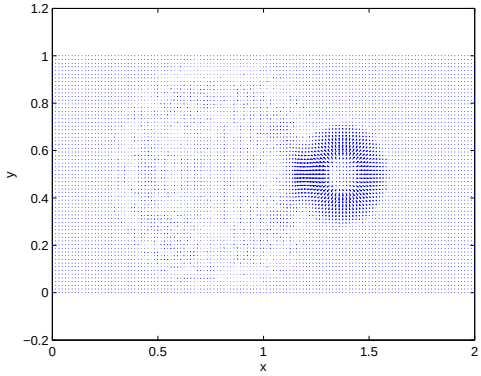

(e) t = 80, whole domain

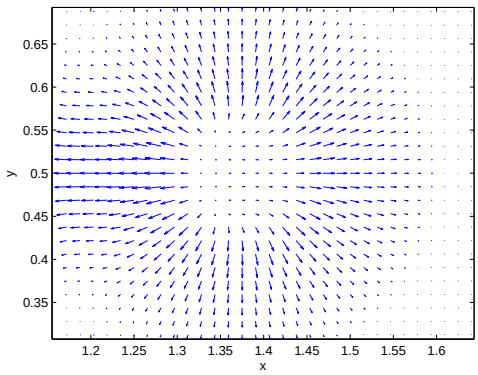

(f) t = 80, zoom in

Figure 6: Flux vector due to chemical potential gradient with initial radius ratio 5:1. The result is obtained from the MCH model.

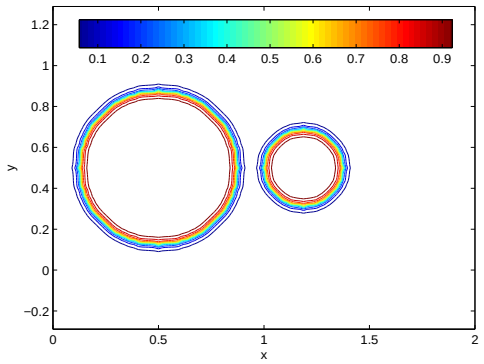

(a) t = 0

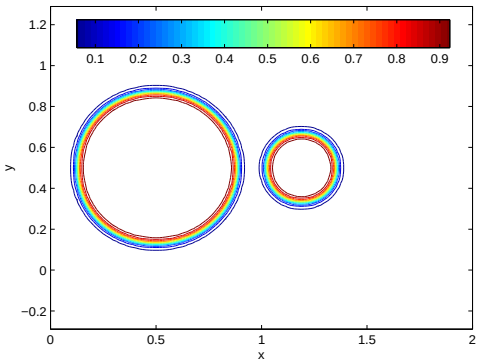

(b) t =200

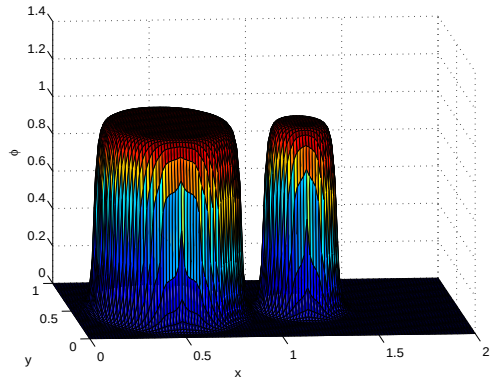

(c) t = 0

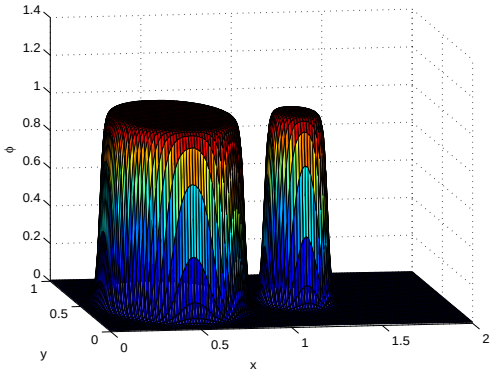

(d) t =200

Figure 7: (a)-(b). Contour plots of two droplets with initial radius ratio 2:1 obtained from the CH model. (c)-(d). Profile of ϕ corresponding to the contour plots in (a) and (b).

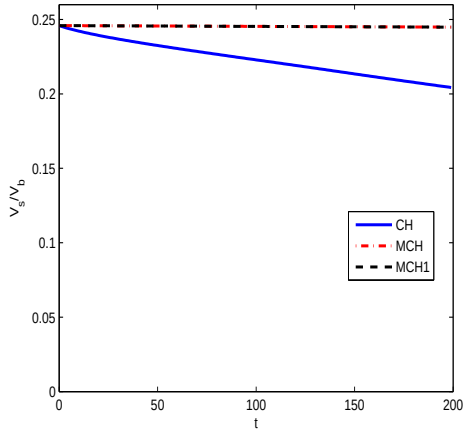

Figure 8: Volume ratio of the smaller to the bigger droplets versus time with the initial radius ratio 1:2.

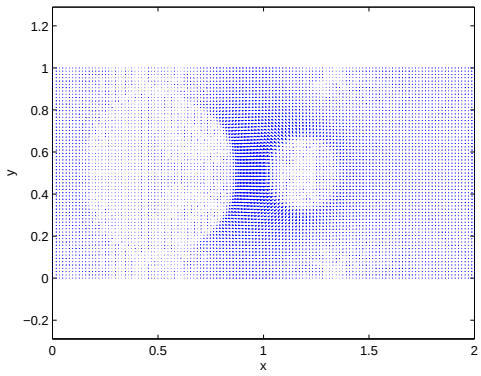

(a) t = 200, whole domain

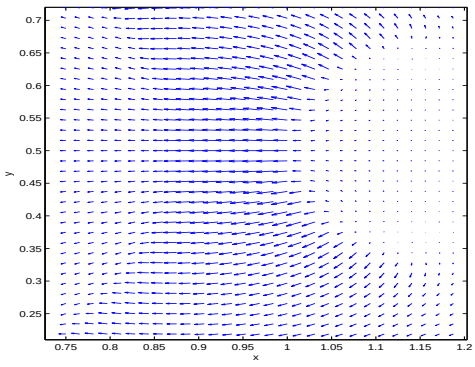

(b) t =200, zoom in

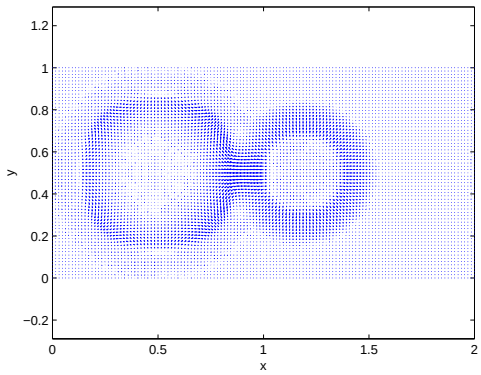

(c) t = 200, whole domain

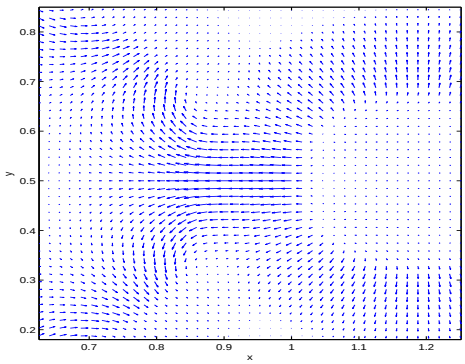

(d) t =200, zoom in

Figure 9: Vector field plot of flux due to chemical potential gradient of initial radius 2:1, (a)-(b). The result of the CH model. (c)-(d). The result of the MCH model.

We next look into a scenario where we increase the radius of the smaller droplet so that the radius ratio of the larger droplet to the smaller one is 2:1. Fig. 7 depicts the simulation with two droplets of the initial radius ratio 2:1 according to the CH model. We notice the shrinking of the smaller droplet is much slower than the case of radius ratio 5:1. There is barely any visible change in the small droplet in the time interval simulated in the MCH models. The volume ratio evolution associated with the droplets is shown in Fig. 8. For the CH model, it decreases linearly at slow rate, dropping about 14% at $t=200$, while for the two MCH models, it barely changes. Fig. 9 depicts the vector field plot of the flux for the CH model and the MCH model at t = 200, respectively. It clearly shows fluxes move from the smaller droplet to the bigger one in the CH model; between the two droplets, the flux forms a pair of vortices that prevent the mass migrates from the smaller one into the larger one in the MCH model, a different flow pattern around the

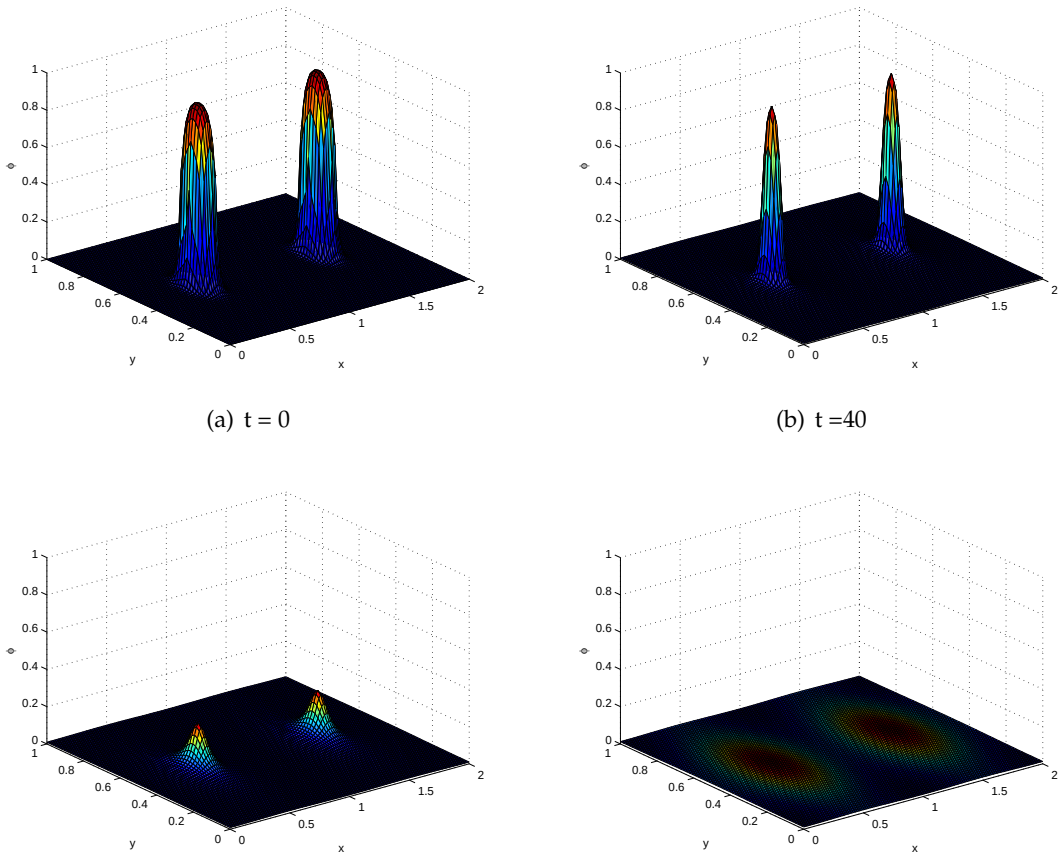

(a) t = 0 (b) t =40

(c) t = 50 (d) t = 60

Figure 10: Time evolution of phase variable ϕ for two droplets with same radius $r=5/64$ up to $t=60$. The profile plot of ϕ is obtained from the CH model.

small droplet. When the two droplets are the same size equal to the radius of the larger droplet in previous numerical experiments, the two droplets do not change visibly in our simulation with any Cahn-Hilliard models even though there are weak mixing going on between the two fluids in the binary fluid.

In the above numerical experiments, we increase the size of the smaller droplet while fixing the size of the larger one. We next reduce the larger droplet to the same size as the smaller one at radius $r=5/64$. Our numerical simulation using the CH model shows that both droplets disappear visibly after $t=60$ hinting that the size of the droplet or the curvature of the interface perhaps matters in the artifact of dissolution of small droplets, (shown in Fig. 10). While we switch to the MCH models, the droplets stay at the time we stop our simulation: $t=200$, shown in Fig. 11. However, if we reduce the size of one of

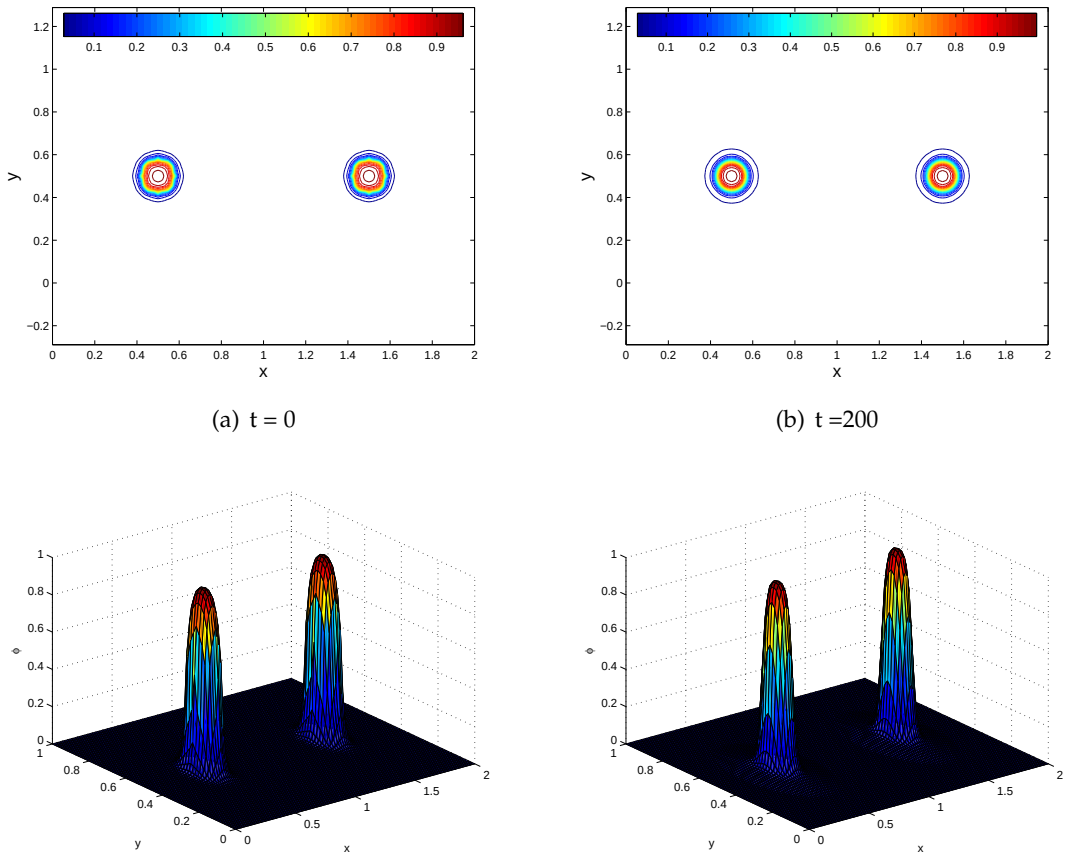

(a) t = 0 (b) t =200

(c) t = 0 (d) t =200

Figure 11: (a)-(b). Contour plots of two droplets with same radius $r=5/64$ obtained from the MCH model. (c)-(d). Profile of ϕ corresponding to the contour plots in (a) and (b).

the droplets by nearly a half, even the MCH can not prevent the dissolution of the smaller droplet. See Fig. 12 for details. We also refine our computational grid in the cases where the droplet either shrinks or dissolves. The outcome seems less sensitive to the uniform mesh refinement. We have not done an adaptive refinement around the interface. We speculate that it may help to eliminate such unwanted dissolution and thereby delay the rate of mass dissipation out of the smaller droplets. This is yet to be confirmed.

In the simulations, the cutoff wave number at $\phi_0=0,1$ is $\sqrt{\frac{2\Gamma_2}{\Gamma_1}}\approx 130.7$ suggested by the linear analysis alluded to earlier. The thickness of the interface is comparable to the reciprocal of the number which is equivalent to one grid size in all calculations. When the droplet size is large, the CH and the MCH models maintain values of $\phi=0,1$ away from the interface nicely; mixing and numerical dissipation is mainly localized in the

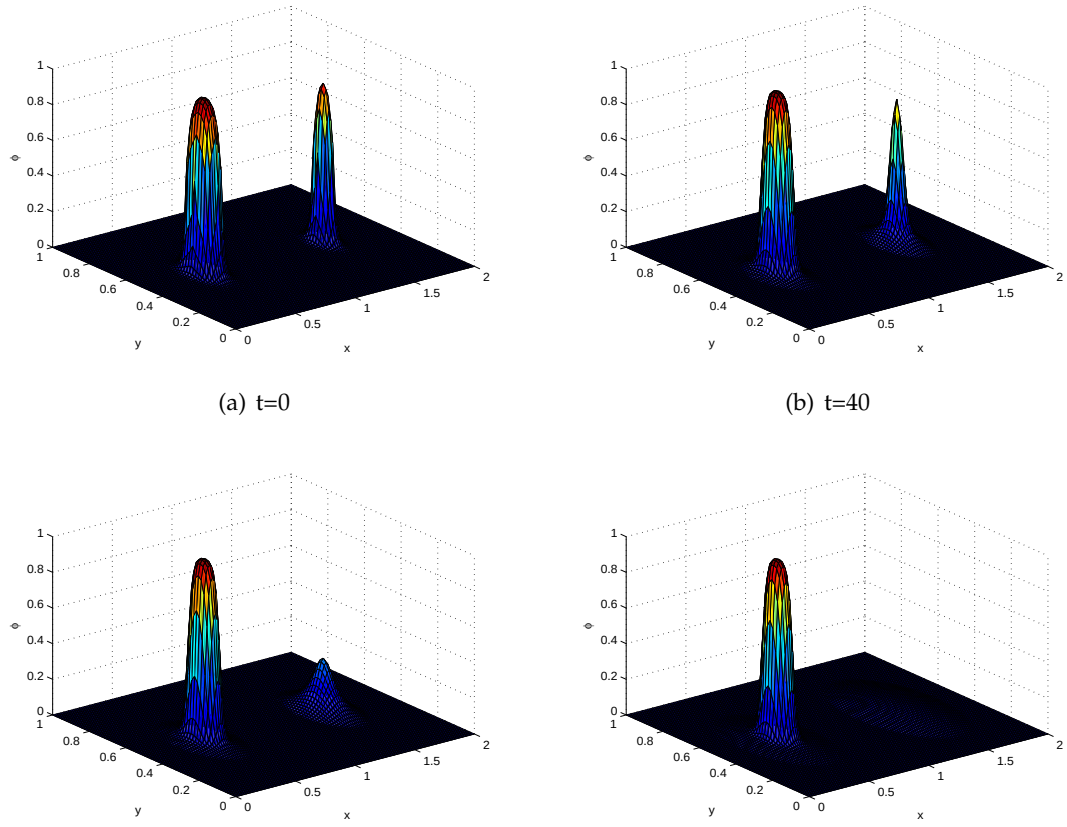

(a) t=0 (b) t=40

(c) t=60 (d) t=200

Figure 12: The profile of ϕ for two droplets with initial radius $5/64$ and $3/64$, respectively up to $t=200$. The result is obtained from the MCH model.

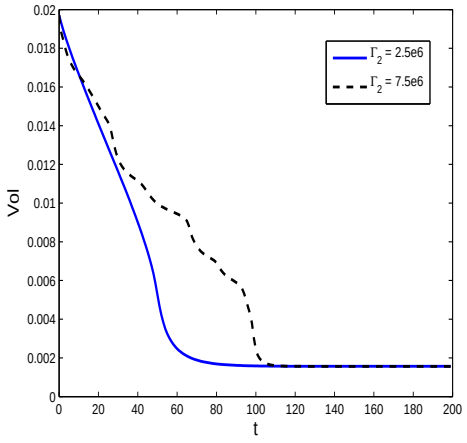

Figure 13: Volume of one droplet calculated using the CH model versus time at different Γ_2 values. Here the radius of the droplet is $r=5/64$ initially.

interfacial region in the time interval we simulated. When the droplet size reduces to the one comparable to a few times of the interfacial thickness, mixing and numerical dissipation inevitably penetrates into the entire droplet. Physical as well as numerical dissipation kicks in simultaneously leading to shrinking of the droplet and the ultimate droplet dissolution. In the modified Cahn-Hilliard models, the transport is cutoff in the bulk phase $\phi = 0$ or $\phi = 1$. As long as a droplet can maintain a sizable interior domain where ϕ=1 is sustainable, the droplet survives in the simulation. As the radius of droplets is comparable to the thickness of the interfacial layer, the entire droplet immerses in the mixing layer; hence, the small droplet fades away in time even in the MCH models just like the small one simulated by the CH model. By enlarging Γ_2 or equivalently reducing the thickness of the interfacial layer, we do observe slowdown in the rate of small droplet dissolution, shown in Fig. 13. However, this also increases stiffness of the system in numerical integration in time, which in turn demands refined meshes.

5 Conclusion

We present some numerical simulations of droplets of a viscous fluid in a second viscous fluid using phase field models consisting of Cahn-Hilliard equations coupled to the Navier-Stokes equation. At appropriate fixed model parameters, the singular Cahn-Hilliard equation tends to resolve the droplet size and interface location better than the Cahn-Hilliard equation. In addition, the singular Cahn-Hilliard equation is physically more relevant for immiscible binary fluids. As the droplet size is comparable to the computational grid size, numerical dissipation, floating point error and strong physical damping collectively contributes to the dissolution of the droplet in intermediate time scales in the phase field modeling, a clear artifact for immiscible droplets. In order to faithfully resolve the small droplet, we surmise that the computational grid size needs to be significantly refined locally around the interface and the model parameters controlling the interface thickness needs to be adjusted to yield a thinner interface. Both of these require significantly refined computational resolution, which perhaps is best achieved by local adaptive computational technology. Within the framework of fixed grid computations, the singular or modified Cahn-Hilliard equations certainly provide better numerical resolution and physical fidelity to the interface problem in multiphase flow simulations for immiscible fluids.

Acknowledgments

Effort sponsored by the Air Force Office of Scientific Research, Air Force Materials Command, USAF, under grant number FA9550-08-1-0107 and the National Science Foundation through grants DMS-0605029, DMS-0626180, DMS-0724273 and CMMI-0825630 are gratefully acknowledged.

References

[1] D. M. Anderson, G. B. McFadden, and A. A. Wheeler, Diffuse-interface methods in fluid mechanics. Annu. Rev. Fluid Mech., 30 (1998), 139-165.

[2] A. N. Beris and B. Edwards, Thermodynamics of Flowing Systems, Oxford Science Publications, New York, 1994.

[3] R. B. Bird, R. C. Armstrong, and O. Hassager, Dynamics of Polymeric Liquids, vol. 1 & 2, John Wiley and Sons, New York, 2987.

[4] J. W. Cahn and J. E. Hilliard, Free energy of a nonuniform system. I: interfacial free energy, J. Chem. Phys., 28, (1958), 258-267.

[5] J. W. Cahn and J. E. Hilliard, Free energy of a nonuniform system. III. Nucleation in a two-component incompressible fluid, J. Chem. Phys., 31, (1959), 688-699.

[6] M. Doi and S. F. Edwards, The Theory of Polymer Dynamics, Oxford Science Publications, Oxford, 1986.

[7] M. Doi, Introduction to Polymer Physics, Oxford Science Publications, Oxford, 1995.

[8] J. Du, B. Fix, J. Glimm, X.-C. Jia, X.-L. Li, Y.-H. Li, and L.-L. Wu, A simple package for front tracking, J. Comput. Phys., 213(2) (2006), 613-628.

[9] P. J. Flory, Principles of Polymer Chemistry, Cornell University Press, Ithaca, NY, 1953.

[10] J. Pyo and J. Shen, Gauge-Uzawa methods for incompressible flows with variable density, J. Comput. Phys., 221 (1) (2007), 181-197.

[11] C. R. Hirt and B. D. Nichols, Volume of uid (VOF) method for the dynamics of free boundaries. J. Comput. Phys., 39 (1981), 201-225.

[12] T. Y. Hou, J. S. Lowengrub, and M. J. Shelley, Boundary integral methods for multicomponent fluids and multiphase materials, J. Comput. Phys., 169 (2) (2001), 302-362.

[13] J. Kim, D. Kim, and H. Choi, An immersedboundary finite-volume method for simulations of flow in complex geometries. J. Comput. Phys., 171(2001), 132-150.

[14] R. J. Leveque and Z. Li, The immersed interface method for elliptic equations with discontinuous coefficients and singular sources, SIAM J. Numer. Anal., 31 (1994), 1001-1025.

[15] C. Liu and J. Shen, A phase field model for the mixture of two incompressible fluids and its approximation by a Fourier-spectral method. Physica D, 179 (2003), 211-228.

[16] S. J. Osher and R. P. Fedkiw, Level Set Methods and Dynamic Implicit Surfaces, Springer-Verlag, 2003.

[17] W. Ostwald, Lehrbuch der Allgemeinen Chemie, vol. 2, part 1. Leipzig, Germany, 1896.

[18] C. S. Peskin, The fluid dynamics of heart valves: experimental, theoretical and computational methods. Annu. Rev. Fluid Mech., 14 (1981), 235-259.

[19] J. A. Sethian, Level Set Methods and Fast Marching Methods Evolving Interfaces in Computational Geometry, Fluid Mechanics, Computer Vision, and Materials Science, Cambridge University Press, 1999.

[20] X.-F. Yang, J. J. Feng, C. Liu, and J. Shen, Numerical simulations of jet pinching-off and drop formation using an energetic variational phase-field method. J. Comput. Phys., 218 (2006), 417-428.

[21] P.-T. Yue, J. J. Feng, C. Liu, and J. Shen, Viscoelastic effects on drop deformation in steady shear. J. Fluid Mech., 540 (2005), 427-437.

[22] P.-T. Yue, J. J. Feng, C. Liu, and J. Shen, A Diffuse-Interface Method for Simulating Two-Phase Flows of Complex Fluids. J. Fluid Mech., 515 (2004), 293-317.

[23] T. Y. Zhang, N. Cogan, and Q. Wang, Phase Field Models for Biofilms. II. 2-D Numerical Simulations of Biofilm-Flow Interaction, Commun. Comput. Phys., 4 (2008), 72-101.